Theory and design of interferometric synthetic aperture radars

E. Rodriguez
J.M. Martin

Indexing terms: Synthetic aperture radar, Interferometry, Global topography

Abstract: Interferometric synthetic aperture radar (InSAR) is a method which may provide a means of estimating global topography with high spatial resolution and height accuracy. The paper presents a derivation of the signal statistics, an optimal estimator of the interferometric phase, and the expressions necessary to calculate the height-error budget. These expressions are used to derive methods of optimising the InSAR-system parameters, and are then used in a specific design example for a system to perform high-resolution global topographic mapping with a one-year mission lifetime, subject to current technological constraints. Finally, a Monte Carlo simulation of this InSAR system is performed to evaluate its performance for realistic topography. The results indicate that this system has the potential to satisfy the stringent accuracy and resolution requirements for geophysical use of global topographic data.

1 Introduction

Global high-resolution digital topographic information is necessary for many geophysical applications, including geology, geomorphology, hydrology, ice studies etc. A study of the resolution requirements [1] has determined that most of the potential applications of such information could use digital topographic maps with spatial resolution on the order of a few tens of metres and vertical resolution on the order of a few metres. This requirement would also satisfy the ice applications if the accuracy of the data could be improved to 10 cm by spatial averaging over 100–500 m^2.

The simultaneous requirements of global coverage, high spatial resolution and high vertical accuracy place severe demands which cannot be met easily with conventional mapping techniques. A potential technique which may meet these requirements, interferometric synthetic aperture radar (InSAR) mapping, has been introduced by Graham [2], Goldstein and Zebker [3] and studied further by Li and Goldstein [4]. This technique uses the relative phase difference between two coherent synthetic-aperture radar (SAR) images obtained by two receivers separated by a crosstrack baseline, to derive an estimate of the surface height. The horizontal resolution of the system is dictated by the SAR bandwidth and antenna length, and can easily be made to satisfy, or exceed, the topographic-resolution requirements. The vertical accuracy of the system is ultimately limited by the SAR-radiation wavelength which, for microwaves, is on the centimetric scale. In addition, InSARs have the capability of providing wide swaths and all-weather performance, in contrast to optical sensors, such as stereo cameras and laser altimeters.

While the theory, design considerations and accuracy of conventional SAR instruments are well known [5], a similar analysis does not exist for InSARs scattering from distributed natural targets. (Moccia and Vetrella [6] have presented an error analysis for point targets, such as corner reflectors. Since, for topographic applications, we are interested in natural targets, which are diffuse scatterers, we restrict our analysis here to extended targets.) In fact, as shown below, an optimal SAR design geared to measuring the radar backscattering cross-section can be far from optimal for measuring topography. An error analysis of InSARs for simplified geometries was presented by Li and Goldstein [4], and they also mentioned the existence of an optimal interferometer baseline. The purpose of the present paper is to extend InSAR theory to include more realistic scattering surfaces and interferometer geometries. Using this theory, we characterise the different error sources for InSARs, and obtain criteria for the selection of optimal InSAR-system parameters.

2 Interferometric-return-signal characteristics

We consider an interferometer system with baseline B, tilted at an angle ξ with respect to the local normal, and with a look angle θ_0. Fig. 1 depicts the scattering geometry. At each of the interferometer receivers, we model the interferometer coherent signal $v_i (i = 1, 2)$ for range r_0 and azimuth x_0 by

$$v_1(r_0, x_0) = A \int dz \int dx\, dy \exp(ikr_1) f(x, y, z) \times W(r_1 - r_0, x - x_0) + n_1 \quad (1)$$

$$v_2(r_0 + \Delta + \delta_r, x_0 + \delta_x) = A \int dz \int dx\, dy \exp(ikr_2) f(x, y, z) \times W\{r_2 - (r_0 + \Delta + \delta_r), x - x_0 - \delta_x\} + n_2 \quad (2)$$

where n_i is the thermal-noise contribution to the signals, k is the wavenumber $(=2\pi/\lambda)$, $W(r, x)$ is the system's range-azimuth-point target response, r_i represents the range from the ith antenna to the scattering point, and A is a coefficient which depends on the system parameters.

Paper 8654F (E15), first received 11th April 1991 and in revised form 6th January 1992

The authors are with the Jet Propulsion Laboratory, California Institute of Technology, 4800 Oak Grove Drive, Pasadena, CA 91109, USA

We have assumed that the signal from the second receiver is offset by a determinstic factor Δ so that it will be coregistered in range with the signal from the first receiver. In addition, we have allowed for the existence of range and azimuth coregistration errors, δ_r and δ_x, respectively.

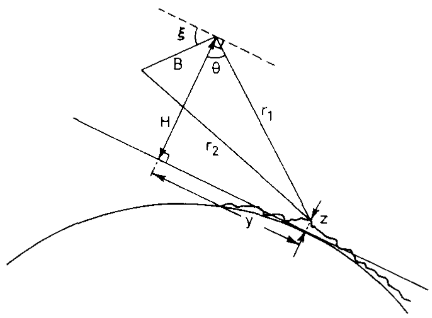

Fig. 1 *InSAR geometry with arbitrary ξ and θ*
H, y and all angles are referenced to the local horizontal plane of the radar target area

Geologic surfaces are generally distributed radar targets which are very rough compared with typical radar wavelengths. These considerations motivate us to assume that the surface scattering amplitude, $f(x, y, z)$, obeys the following equation

$$\langle f(x, y, z) f^*(x', y', z') \rangle = \sigma_0(x, y, z, \theta)\delta(x - x')\delta(y - y')\delta(z - z') \quad (3)$$

where $\sigma_0(x, y, z, \theta)$ is the normalised backscatter cross-section unit height for incidence angle θ. The assumption that the surface scattering amplitude has a delta-function correlation is consistent with the deep-phase approximation in scattering theory [7], which applies to surfaces whose root-mean-square height is much larger than the incident radar wavelength. Notice that the more common normalised radar cross section is defined as

$$\sigma_0(x, y, \theta) = \int dz\, \sigma_0(x, y, z, \theta) \quad (4)$$

If the SAR coherent return signal has circular Gaussian statistics, as is often observed, a complete characterisation of the interferometric return can be obtained by calculating the complex covariance matrix for v_1 and v_2. Using eqn. 3, and the fact that n_1 and n_2 are uncorrelated, the complex covariance of v_1 and v_2 is given by

$$\begin{aligned}\langle v_1(r_0 x_0) v_2^*(r_0 + \Delta + \delta_r, x_0 + \delta_x) \rangle &= A^2 \int dz \int dx\, dy \exp\{-ik(r_1 - r_2)\} \\ &\times \sigma_0(x, y, z, \theta) W(r_1 - r_0 x - x_0) \\ &\quad W^*(r_1 - r_0 - \Delta - \delta_r, x - x_0 - \delta_x) \end{aligned} \quad (5)$$

To make further progress, we approximate

$$r_2 - r_1 \simeq \Delta + \frac{B_\perp}{r_0}(\eta \cos \theta_0 + \zeta \sin \theta_0) \quad (6)$$

$$\frac{\Delta}{r_0} = \sqrt{\{1 + 2B \sin(\theta_0 - \xi)/r_0 + (B/r_0)^2\}} - 1 \quad (7)$$

$$\simeq \mathrm{B} \sin(\theta_0 - \xi)/r_0 \quad (8)$$

$$B_\perp = B \cos(\theta_0 - \xi) \quad (9)$$

where $B_\perp$ is the projection of the interferometric baseline onto the direction perpendicular to the look direction, $\eta = y - y_0$, and $\zeta = z - z_0$. We decompose the scatterer height locally into a tilted-plane component and an additional component w representing the height above the mean tilted plane

$$\zeta = (x - x_0) \tan \tau_x + \eta \tan \tau_y + w \quad (10)$$

where τ_x and τ_y represent the surface slopes in the x and y directions, respectively.

As a likely characteristic of natural targets, we assume that, at least in the neighbourhood of x_0 and y_0, the surface brightness is homogeneous, and that the scatterer properties are only governed by their height above the mean tilted plane

$$\sigma_0(x, y, z, \theta_0) = \sigma_0(w, \theta_0) \quad (11)$$

We expect this assumption to be good for most natural targets which have no sharply defined changes in surface brightness. This assumption is not as good for some inhabited areas, where sudden changes in the reflectivity are common.

Finally, we choose the SAR system point-target response to be given by

$$W(r, x) = \mathrm{sinc}\left(\frac{\pi r}{R}\right) \mathrm{sinc}\left(\frac{\pi x}{X}\right) \quad (12)$$

where $\mathrm{sinc}\,(x) = \sin(x)/x$; R is the intrinsic range resolution, given by $c/(2\Delta f)$, where c is the speed of light and Δf is the system bandwidth; and X is the SAR azimuth resolution, given by $L/2$ for full-aperture synthesis, where L is the antenna length.

After some tedious algebra, eqn. 5 can be integrated analytically to obtain the complex covariance

$$\langle v_1 v_2^* \rangle = A^2 S \sigma_0(r_0, x_0, \theta_0) \exp(-ik\Delta)\alpha \quad (13)$$

$$\begin{aligned}\alpha &= \tilde{\sigma}_0(a_z, \theta_0)(1 - |a_r R|) \exp(-i\pi a_r \delta_r) \\ &\times \mathrm{sinc}\left\{\pi \frac{\delta_r}{R}(1 - |a_r R|)\right\} \\ &\times (1 - |a_x X|) \exp(-i\pi a_x \delta_x) \\ &\times \mathrm{sinc}\left\{\pi \frac{\delta_x}{X}(1 - |a_x X|)\right\}\end{aligned} \quad (14)$$

$$a_r = \frac{kB_\perp}{2\pi r_0 \tan(\theta_0 - \tau_y)} \quad (15)$$

$$a_z = \frac{kB_\perp \cos \tau_y}{r_0 \sin(\theta_0 - \tau_y)} \quad (16)$$

$$a_x = \frac{a_z \tan \tau_x}{2\pi} \quad (17)$$

where S is the area of the SAR resolution element, and $\tilde{\sigma}_0(a_z, \theta_0)$, the normalised Fourier transform of the radar cross-section as a function of height, is defined as

$$\tilde{\sigma}_0(a_z, \theta_0) = \frac{1}{\sigma_0(r_0, x_0, \theta_0)} \times \int dw \exp(-ia_z w)\sigma_0(w, \theta_0) \quad (18)$$

When surface slope and misregistration can be neglected, notice that $1 - \alpha$, the geometric decorrelation, is directly proportional to $B_\perp/r_0$, the angle subtended by the baseline viewed from the surface, and inversely proportional to the wavelength.

A similar derivation to that shown above yields

$$\langle |v_1|^2 \rangle = \langle |v_2|^2 \rangle = A^2 S \sigma_0 + N \tag{19}$$

where N is the mean thermal-noise power (assumed to be equal in both receivers). This implies that the correlation coefficient between the two signals is given by

$$\gamma = \frac{|\langle v_1 v_2^* \rangle|}{\sqrt{\{\langle |v_1|^2 \rangle \langle |v_2|^2 \rangle\}}} = \frac{|\alpha|}{1 + R_{SN}^{-1}} \tag{20}$$

where R_{SN} is the system signal to noise ratio. Notice that in the infinite R_{SN} limit, the correlation is given by $|\alpha|$, which we call the geometric correlation, since it depends only on geometric parameters. This correlation function is the extension of the usual van Cittert-Zernike theorem [8] to scatterers distributed in three dimensions. The results presented above reduce in the limit of a flat surface, no azimuth-coregistration error, no surface tilt, and no baseline tilt, to those presented by Li and Goldstein [4]. Their parameter δ, the decorrelation, is defined as $\delta = 1 - \gamma$.

If the phase of α is zero, the mean phase difference $-k\Delta$ between the two SAR signals is the interferometric phase difference resulting from the path difference between the point (x_0, y_0, z_0) and the two extremities of the interferometer baseline. This implies that in the mean, provided that the phase of α is zero, the interferometric phase from a distributed target is equivalent to the interferometric phase from a point target located exactly at the centre of the SAR resolution cell. This is equivalent to saying that, for a flat distributed target the mean phase centre of the target lies at its geometric centre, a result which is intuitively clear from symmetry considerations. This implies that one can use the interferometric phase from distributed targets to calculate unambiguously the height of the centre of the distributed resolution cell, provided that α has zero phase.

The phase of α can be nonzero for two reasons. First, either range or azimuth coregistration errors can induce a nonzero phase, as can be seen by inspecting eqn. 14. If the interferometer geometry is known, this phase can be made very small since the SAR signals can be coregistered to a small fraction of a resolution cell size.

Secondly, the normalised Fourier transform of the scattering cross-section as a function of height can have a nonzero phase. This will happen whenever $\sigma_0(w)$ is not symmetric about $w = 0$. We present two simple models for $\sigma_0(w)$: one appropriate for bare geologic surfaces; another for surfaces covered by vegetation.

In the first case, we expect the cross-section to be due to specular points which closely follow the topography within the resolution cell. If the topography is approximately Gaussian, $\tilde{\sigma}_0$ can be modelled as [9]

$$\tilde{\sigma}_0(a_z, \theta_0) = \frac{1}{\sqrt{(2\pi\sigma_s)}} \times \exp\left\{-ia_z z_{EM} - \frac{a_z^2 \sigma_s^2}{2} - i\frac{\lambda_s}{6}(a_z\sigma_s)^3\right\} \tag{21}$$

where z_{EM} is the specular point mean height, σ_s is the specular point standard deviation, λ_s is the specular point skewness, and it is implicitly assumed that the parameters of the of the distribution are functions of θ_0.

Ignoring the skewness contribution, it is easy to see that the phase contribution will induce a height error of z_{EM} in the estimated height. This shift of the electromagnetic mean level with respect to the mean topography is well known in oceanography, where it is called the 'electromagnetic bias' [9]. It is typically quite small compared with the accuracies required for topographic mapping. Note that, in addition to providing a possible phase shift, the vertical distribution of scatterers causes a decrease in the geometric correlation: the geometric correlation decreases as the vertical variance of the scatterers increases. The magnitude of this decrease, and its effect on height estimation, will be treated below for a specific interferometric design.

To model vegetation cover, we assume a scattering cross-section as a function of height of the form

$$\sigma_0(w) = \exp(-\beta w_t)\sigma_{0\,ground}\,\delta(w) + \sigma_{0\,tree}\frac{\beta}{1 - \exp(-\beta w_t)} \times \exp\{-\beta(w_t - w)\} \tag{22}$$

for $0 \le w \le w_t$, and zero otherwise. The parameter β, which is a function of incidence angle and vegetation type, accounts for the radiation attenuation due to the scattering and absorption from the vegetation. The normalised Fourier transform of this function is easily computed:

$$\tilde{\sigma}_0 = \frac{e^{-\mu}\sigma_{0\,ground} + \sigma_{0\,tree}\,\mu e^{-\mu}/(1 - e^{-\mu}) \times \{\exp(\mu - iv) - 1\}(\mu - iv)}{e^{-\mu}\sigma_{0\,ground} + \sigma_{0\,tree}} \tag{23}$$

where $\mu = \beta w_t$ and $v = a_z w_t$. It can be seen that by varying the value of β one can make the scattering phase centre, and hence the interferometer height bias, lie anywhere between 0 (when no vegetation is present) and w_t (when the attenuation becomes very large). The magnitude of the correlation coefficient is seen to be inversely proportional to $1/\beta$, the penetration depth, or w_t the vegetation height, depending on which is smaller.

3 Interferometric phase estimation

Due to speckle, it is not advantageous to estimate the interferometric phase using one-look SAR data. Rather, increased accuracy can be obtained by combining the returns from several interferometric pairs of equal mean phase (or height). It has been shown in Reference 10 that, for homogeneous targets, the maximum-likelihood estimator (MLE) of interferometric phase from distributed targets is given by

$$\hat{\Phi} = \arctan\left[\frac{\mathrm{Im}\{\sum_{n=1}^{N_L} v_1^{(n)} v_2^{*(n)}\}}{\mathrm{Re}\{\sum_{n=1}^{N_L} v_1^{(n)} v_2^{*(n)}\}}\right] \tag{24}$$

where N_L is the number of looks to be averaged.

The MLE estimator is unbiased modulo 2π, and the phase variance can easily be obtained numerically, as shown by Li and Goldstein [4]. Fig. 2 presents a plot of the phase standard deviation as a function of the decorrelation parameter δ for various numbers of looks. The Cramer-Rao bound [10] for the phase-standard deviation was shown to be given by

$$\langle(\hat{\Phi} - \langle\hat{\Phi}\rangle)^2\rangle^{1/2} = \frac{1}{\sqrt{(2N_L)}}\frac{\sqrt{(1 - \gamma^2)}}{\gamma} \tag{25}$$

The phase standard deviation approaches this limit asymptotically as the number of looks increases. Fig. 3 presents a comparison of the actual phase-standard deviation against the Cramer-Rao bound for various values of the decorrelation parameter. As can be seen, the phase-standard deviation decreases much faster than $N_L^{-1/2}$ for the first four looks, especially if the correlation is high. After that, the phase-standard deviation can be approximated by the Cramer-Rao bound. The fact that the phase-standard deviation decreases quickly with the first four looks indicates that at least that many looks should always be taken when estimating the interferometric phase.

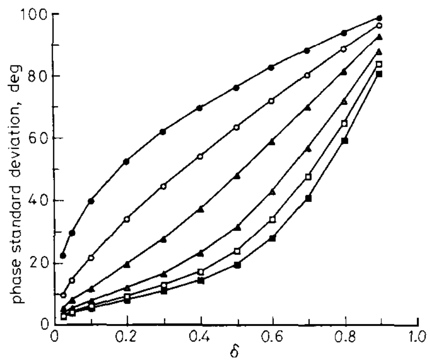

Fig. 2 *Standard deviation of phase difference between two images against decorrelation $\delta = 1 - \gamma$ for N_L varying between 1 and 16 looks*

For small δ, the phase variation decreases vary rapidly with looks for the first four looks. These results calculated using 100 000 realisations in a Monte Carlo simulation similar to that described in Reference 4

—●— 1 look
—○— 2 looks
—▲— 4 looks
—△— 8 looks
—■— 16 looks
—□— 12 looks

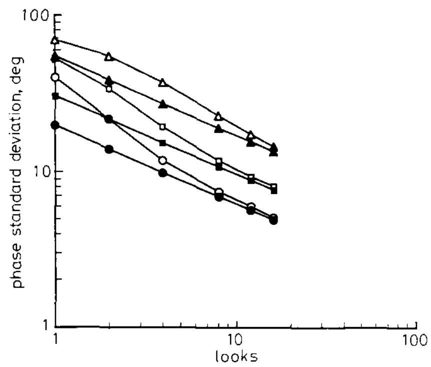

Fig. 3 *Comparison of phase standard deviation calculated by Monte Carlo and from Cramer-Rao bound/maximum-likelihood method for $\delta = 0.1, 0.2$ and 0.4 against number of looks*

MLE result closely approaches Monte Carlo result for $N_L > 4$

—○— delta = 0.1
—●— MLE delta = 0.1
—□— delta = 0.2
—■— MLE delta = 0.2
—△— delta = 0.4
—▲— MLE delta = 0.4

4 Interferometer height-error budget

From Fig. 1, one can see that the height z and location x of a surface point above a local tangent plane can be obtained by means of the equations

$$
\begin{aligned}
z &= H - r\cos\theta \\
&= H - r[\cos\xi\sqrt{\{1 - \sin^2(\theta - \xi)\}} \\
&\quad - \sin\xi\sin(\theta - \xi)]
\end{aligned}
\tag{26}
$$

$$y = r\sin\theta \tag{27}$$

where H is the interferometer height above the plane, r is the range from the first antenna to the point, and θ is the look angle. The height H is obtained from knowledge of the orbit, and r, half the round-trip distance, is obtained from the SAR internal clock. (Notice that in a SAR interferometer, r is not a range to be estimated, as in conventional altimeters. Rather, it represents the sampling time of the compressed return signal, and its accuracy is that of the SAR reference clock. The reason r need not be estimated is that, as we saw in the last Section, for distributed targets the return phase can be assigned to the centre of the resolution cell.) The local incidence angle is obtained by calculating

$$\sin(\theta - \xi) = \frac{(r + \Delta)^2 - r^2 - B^2}{2Br} \tag{28}$$

where $\hat{\Phi}$ is the estimated interferometric phase difference, and $\Delta = -\hat{\Phi}/k$.

We distinguish between two types of error in estimating topography. The first type, which we call intrinsic height error, is due to errors in estimating the height z in eqn. 26. The second type, which we call location-induced errors, are due to the fact that the correct height is reported at the wrong location. If δy (or δx) is the location error, then the induced-height error, δz is given by $\delta z = \delta y \tan\tau_y$ (or, $\delta z = \delta x \tan\tau_x$).

The sensitivity of the estimated height to errors in knowledge of the various interferometer parameters, or to phase errors, can be obtained by differentiating eqns. 26–28 with respect to the various system parameters. The results are given in the following equations (which incorporate both intrinsic and induced height errors)

$$\delta z_B = -r\tan(\theta - \xi)(\sin\theta + \cos\theta\tan\tau_y)\frac{\delta B}{B} \tag{29}$$

$$\delta z_\xi = r(\sin\theta + \cos\theta\tan\tau_y)\delta\xi \tag{30}$$

$$\delta z_{\hat{\Phi}} = \frac{r(\sin\theta + \cos\theta\tan\tau_y)}{kB\cos(\theta - \xi)}\delta\hat{\Phi} \tag{31}$$

$$\delta z_r = -\cos\theta\,\delta r \tag{32}$$

$$\delta z_H = \delta H \tag{33}$$

$$\delta z_x = \tan\tau_x\,\delta x \tag{34}$$

In the previous equations, the location-induced height errors are the ones proportional to the surface slope. Notice that the surface and scatterer characteristics only affect the intrinsic height errors through $\delta\hat{\Phi}$, which is due to phase biases or to changes in the geometric correlation.

Another useful way of characterising height errors is by the corrections which have to be made to the derived topography to rectify them. We identify three kinds of errors:

(i) *Random errors:* These are errors which are independent from pixel to pixel. They cannot be removed by using tie points. On the other hand, in the absence of phase biases (as in the presence of vegetation), they can be reduced by averaging, at the expense of horizontal resolution. For the interferometer, these are the errors due to estimation noise on the interferometric phase. These errors determine the precision of the interferometric system, while the following errors determine the accuracy.

(ii) *Geometric distortion:* These are deterministic long-wavelength errors which, in general, cannot be removed by vertical or horizontal shifts of the topography. However, they may be removed by using two, or more, tie points. These errors include:

(*a*) Attitude errors: an error in the attitude induces, to first order, a height shift and a linear tilt of the topography in the crosstrack direction. It can be corrected by using two tie points.

(*b*) Baseline errors: an error in the estimated interferometer baseline induces, to first order, a height shift and a quadratic surface distortion in the crosstrack direction. It can be corrected by using three tie points.

(*c*) Clock timing errors (or atmospheric delay): these errors have similar characteristics to baseline errors.

If the interferometer swath is small enough, it may be possible to correct for the bulk of these errors using only one tie point, since the residual geometric distortions are then small.

(iii) *Position errors:* These errors may be removed by a simple vertical or horizontal shift in the topography. They include orbit error and SAR-processing azimuth-location errors. Correction of these errors requires only one tie point.

5 Interferometer-design optimisation

Given the height sensitivities derived in the previous Section, it is possible to minimise the height error by choosing an optimal set of system parameters. In general, this involves searching for a minimum in a space of many dimensions, which is often difficult. In this Section, we show that by optimising one parameter at a time, while holding the other system parameters fixed, one is able to arrive at a set of general guidelines for achieving close-to-optimal interferometer performance. (In the following analysis, we assume that coregistration errors and surface-induced errors can be ignored.)

Baseline-tilt optimisation

It is obvious from eqn. 29 that if we choose $\xi = \theta_0$, the δz_B vanishes at the centre of the swath. In the low-R_{SN} limit, γ and thus $\delta\hat{\Phi}$ are independent of ξ, so

$$\delta z_{\hat{\Phi}} \propto \cos^{-1}(\theta - \xi)$$

In the high R_{SN} limit $\gamma \sim |\alpha|$, so

$$\delta\hat{\Phi} \propto \frac{\sqrt{(1/\gamma^2)}}{\gamma} \propto \cos^{1/2}(\theta - \xi)$$

and

$$\delta z_{\hat{\Phi}} \propto \cos^{-1/2}(\theta - \xi)$$

Hence, we conclude that $\delta z_{\hat{\Phi}}$ is also minimised by choosing ξ equal to the interferometer look angle. We note that, if the interferometer baseline is not tilted, constraining the baseline error places extremely stringent requirements on the measurement for the interferometer baseline. These requirements are relaxed at least an order of magnitude by tilting the baseline to the optimum angle.

Optimum bandwith (or geometric correlation)

Increasing the system bandwidth decreases the geometric decorrelation [proportional to $(\Delta f)^{-1}$] and increases the number of looks (proportional to Δf) and hence, in the high-R_{SN} limit, decreases the height error. On the other hand, it decreases the R_{SN} [proportional to $(\Delta f)^{-1}$], so that in the low R_{SN} limit, the height error is increased by increasing the bandwidth. Therefore, an optimum bandwidth must exist.

It is not possible to minimise the height error analytically with respect to the bandwidth, since this involves solving a 5th-order polynomial equation. However, an examination of the height error as a function of bandwidth (or, equivalently, geometric correlation) clarifies the criterion for optimum bandwidth. As the bandwidth changes, the parameter $\rho = (1 - \alpha)/R_{NS}$ remains constant. Typically, $\rho \ll 1$. In Fig. 4 we plot the normalised height

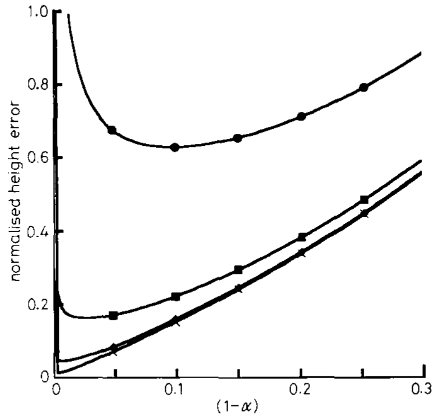

Fig. 4 *Normalised height error $\delta z_{1\,norm}$ as a function of geometric decorrelation $(1 - \alpha)$*

Bandwidth is inversely proportional to $(1 - \alpha)$, so this plot implies a very large optimal bandwidth

● $\gamma = 10^{-1}$
■ $\gamma = 10^{-2}$
◇ $\gamma = 10^{-3}$
× $\gamma = 10^{-4}$

error

$$\delta z_{1\,norm} = \sqrt{\left(\frac{2YkB_\perp \cos\theta}{2\pi r}\right)} \frac{kB_\perp}{r \sin\theta}\,\delta z \tag{35}$$

(Y is the ultimate ground resolution in the y direction) as a function of $(1 - \alpha)$ for various values of ρ. It is clear from this Figure that the optimum values of $(1 - \alpha)$ are very small for typical values of ρ. This implies that to increase the geometric correlation one should in general increase the system bandwidth as much as the data-rate constraints will allow.

Baseline-length (or correlation) optimisation

It is clear from eqn. 31 that the height error diverges as the baseline length approaches zero. On the other hand, if the baseline is too large the correlation between the two SAR returns approaches zero because of the van Cittert-Zernike theorem, and the phase noise diverges. Hence, an optimum baseline must exist. This statement is equivalent to saying that an optimum correlation between the interferometer returns exists since, all other parameters being equal, there is a linear relation between these two parameters. To find the optimum correlation, we minimise the height error by taking the derivative of eqn 31 with respect to the correlation and setting the result to zero. The optimum correlation is given by

$$\gamma_{opt} = \frac{[\sqrt(-3)](3x^2 - 2) + 2 + 3x^2}{6x} \tag{36}$$

$$x = \left\{\frac{\epsilon}{2} + \sqrt{\left(-\frac{8}{27} + \frac{\epsilon^2}{4}\right)}\right\}^{1/3} \tag{37}$$

$$\epsilon = R_{SN}/(R_{SN} + 1) \tag{38}$$

Typically, SARs are designed such that $R_{NS} \ll 1$. One can therefore expand γ_{opt} to obtain the 'golden rule' of interferometric design:

$$\gamma_{opt} \simeq \phi - 1 - 1.171 R_{SN}^{-1} \tag{39}$$

where $\phi = 1.618\ldots$ is the golden mean. Expr. 39 predicts that, for a finite R_{SN}, optimum performance is achieved by selecting the interferometric baseline to be longer than the infinite R_{SN} optimum baseline.

This value of γ conflicts with the very small values of $(1 - \alpha)$ required for bandwidth optimisation in the large limit. Given an initial baseline and bandwidth, if we successively optimise both quantities they both increase until the resolution approaches the electromagnetic wavelength. We can see this by combining eqns. 20, 25 and 31 to obtain

$$\delta z_{\hat{\Phi}} \simeq \frac{1}{B[\sqrt(\Delta f)]} \frac{1 + R_{SN}^{-1}(\Delta f/\Delta f_0)}{1 - (1 - \alpha_0)(B/B_0)(\Delta f_0/\Delta f)} \tag{40}$$

where the subscripted quantities are those of the reference system and the unsubscripted refer to variable quantities B and Δf. If we assume that $B \propto \Delta f$, it can be shown that, as Δf is allowed to increase without bound, both γ and $\delta z_{\hat{\Phi}}$ go to 0. This strategy cannot be applied in practice, of course, since other limits become important, i.e. the allowable decorrelation is limited by the requirements for successful phase unwrapping, the bandwidth is limited by the maximum allowable data rate or onboard processing speed, and the baseline is limited by structural considerations. Given a maximum bandwidth, however, the optimum baseline may be chosen using the 'golden rule' above.

To study the interferometric SAR sensitivity to baseline selection, the normalised height error, defined as

$$\delta z_{2\,norm} = \frac{2\pi[\sqrt(N_L)]\delta z}{R \cos\theta} \tag{41}$$

is plotted in Fig. 5. As can be seen, the optimum performance is obtained when the correlation obeys expr. 39. However, the height performance is not very sensitive to the choice of baseline, and a range of baselines will give similar performance. (Since eqn. 25 underestimates the phase standard deviation somewhat for the smaller values of the correlation, the actual height error will diverge slightly more rapidly in this regime, and the height error will be more sensitive to correlation than shown in the Figure. However, the basic shape of the curve is preserved. Eqn. 25 works well about the optimum point.) This range decreases as R_{SN} decreases. A good rule of thumb seems to be that the InSAR system should be designed, if mechanically possible, such that the correlation coefficient is between 0.5 and 0.6. This will provide the least degradation with decreasing SNR.

Optimum antenna length (or number of looks)
In the high-R_{SN} limit, decreasing the antenna length increases the number of looks (proportional to L^{-1}) and therefore reduces the phase noise. On the other hand, as the low-R_{SN} limit is reached, decreasing the antenna length decreases R_{SN} (proportional to L^2 since we assume the longest possible pulse, and the minimum PRF goes like L^{-1}) and increases the phase noise. We conclude that an optimal antenna length, or, equivalently, an optimal number of looks, exists.

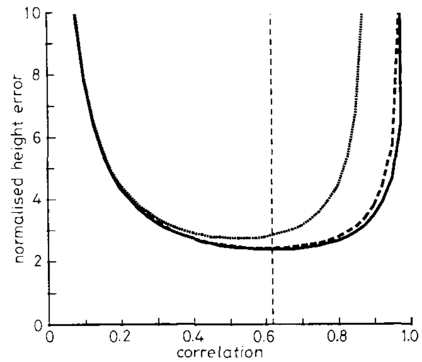

Fig. 5 *Normalised height error $\delta z_{2\,norm}$ against γ for $R_{SN} = 10$ dB, 20 dB and infinity*
Optimal value of γ for infinite R_{SN} is $\phi - 1$, where ϕ is the golden mean. The rather broad bottom of these results indicates that a wide range of γ will yield near-optimal height error
—— infinite R_{SN} ---- 20 dB R_{SN} .... 10 dB R_{SN}

As the antenna length changes, the parameter $\chi = N_L R_{SN}^{1/2}$ remains constant. Typically, $\chi \gg 1$ for most interferometric systems. Defining $u = (N_L/\chi)^2 = 1/R_{SN}$, one easily obtains an optimum value for u by differentiating eqn. 31, and setting the result equal to zero:

$$u_{opt} = \frac{1}{R_{SN\,opt}} = \frac{\sqrt{\{1 + 3(1 - \alpha^2)\}} - 1}{3} \tag{42}$$

In the limit of high geometric correlation, this can be simplified to $R_{SN\,opt} \simeq 1/(1 - \alpha)$, or $N_{L\,opt} = \chi\sqrt(1 - \alpha)$.

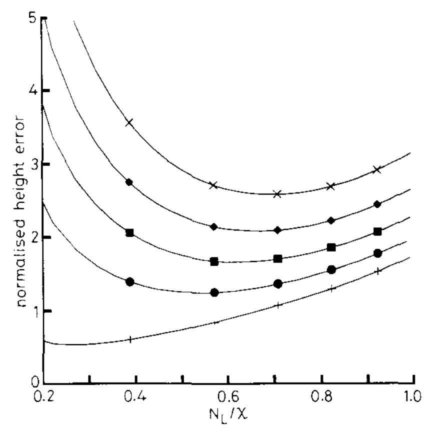

Fig. 6 *Normalised height error $\delta z_{3\,norm}$ against N_L/χ*
For a given decorrelation and χ, these plots yield the optimal number of looks, or equivalently the optimal antenna length, since $L \propto 1/N_L$
+ $(1 - \alpha) = 0.05$
● $(1 - \alpha) = 0.1$
■ $(1 - \alpha) = 0.2$
● $(1 - \alpha) = 0.3$
× $(1 - \alpha) = 0.4$

Fig. 6 presents the normalised height error

$$\delta z_{3\,norm} = \chi^{1/2} \frac{(\sqrt{2})kB_\perp}{r \sin\theta} \delta z \tag{43}$$

as a function of N_L/χ, for various values of the geometric correlation. As can be seen, it is very advantageous to increase the number of looks to the optimum, and the height error degrades more gracefully if too many looks are taken than if too few looks are taken. This is especially true if geometric correlation is close to one, as is the case if the bandwidth has been optimised.

6 Design example

The following sample design shows how one may employ the analytic relations to rationally minimise the height error within constraints imposed by physical structure, power, weight, data rate etc. The objective is to measure the earth's topography with a ground resolution of 30 × 30 m and a height precision of <3 m in a period less than one year. We assume that, due to the demand on TDRSS (Tracking and Data Relay Satellite System), our data rate must be substantially less than the projected capability of TDRSS, which will be of the order of 500 Mbit/s. Assuming that a safe average data rate is of the order of 50 Mbit/s, and allowing for the fact that land makes up approximately 40% of the earth's surface, we conclude that an instantaneous data rate around 100 Mbit/s is the maximum allowable.

As an additional constraint, and to minimise the required transmitter power and launch vehicle expense, we assume that the mission will be flown in a 400 km high polar orbit. We have identified orbits that will allow full global coverage (twice) in less than one year at this height, provided that the InSAR swath is greater than 10 km.

The choice of operating frequency is determined mainly by the physical limits to the allowable baseline separation. If we assume a single-spacecraft design (which has substantial cost and simplicity advantages), 10–20 m is about all that can be reasonably expected. We can rearrange eqn. 20 using the optimum γ_{opt} to find the optimum frequency for a given baseline

$$\lambda_{opt} = \frac{RB_\perp}{r_0 \tan\theta_0 \{1 - \gamma_{opt}(1 + R_{SN}^{-1})\}} \tag{44}$$

which yields an optimum wavelength on the order of 1 mm for a baseline of 12 m, an orbit altitude of 400 km, and a look angle of 30°, and large R_{SN}. Clearly, the optimum frequency for this design is the highest for which we can build powerful amplifiers and sensitive receivers, and which is not seriously degraded by clouds and water vapour in the atmosphere. For technical reasons, then, the operating frequency was determined to be 35 GHz. Note that even though our operating γ is significantly higher than the optimum value, we can still obtain excellent performance, as shown below.

We mention that another possible approach is to assume that two spacecraft may be used to implement the interferometer geometry. Such a possibility can be implemented either as two tethered spacecraft [6], or using repeat passes from a single spacecraft [4]. Since typical baseline lengths in this case are of the order of 1 km, the optimum frequency for these configurations is much lower. We have not chosen the first design approach because the need for two attitude-stabilised tethered spacecraft increases the complexity, and hence the cost, of the system. We also notice that the tether geometry (where the baseline tilt approaches 90°) is the least optimal according to the analysis above if the incidence angle is less than 45°. The fact that the baseline is not at the optimal tilt also puts significant constraints on the accuracy with which it must be measured. The repeat-track option, on the other hand, has the advantage that it requires only one radar, but suffers from the potentially significant disadvantage that the ground surface may change from pass to pass, and the two images may not correlate. The amount of degradation between passes is a subject of current research and a major unknown.

Several other constraints must also be imposed on this system which will influence the choice of design parameters. The swath must be as large as possible, and be at least 10 km to obtain global coverage in less than a year. The look angle θ_0 must be as large as possible to reduce the incidence of image layover, which can produce significant problems in phase unwrapping [11] as well as a loss of height information in the laid-over regions. On the other hand, θ_0 must not be so large as to produce an unmanageable data rate, significant shadowing, or an uunacceptable loss in signal-to-noise ratio due to angular variation of σ_0. Optimising these design choices is not an easy task, as the requirements on data rate and swath are mutually incompatible, and optimisation on a single quantity (such as height error) is not possible. These requirements define a space of possible choices, and the best procedure is to assume several combinations, derive the data rates and swaths, and discover some acceptable set. For our example, we have chosen $\theta_0 = 30°$, since that slope is rarely sustained over a 30 m resolution element;† and the minimum swath of 10 km, as we find that our instantaneous data rate for this case is less than the maximum allowable of 100 Mbits. This swath determines the antenna width of 0.45 m. We already known from the previous Section that the optimum baseline orientation is $\xi = \theta_0$. Available technology or spacecraft-power limits generally determine the transmitted power of the radar, and in our case we are limited by current 35 GHz TWT amplifier technology to about 250 W of output power.

Given that the above parameters are fixed by constraints, there are still a number of parameters which may now be optimised to minimise the height error, such as antenna length L (or equivalently, the number of azimuth looks) and the chirp bandwidth Δf. In addition, it is often useful to know how the system would perform if some of the constraints were to be relaxed, e.g. if power or data bandwidth could be increased. To see the effects of these parameter changes clearly, we plot in Fig. 7 the height-error performance as a function of L, B, Δf and σ_0 keeping all other parameters constant. These plots may be most easily constructed by calculating the α, γ, $\delta\hat{\Phi}$, and $\delta z_{\hat{\Phi}}$ from eqns 14, 20, 25 and 31 for a given reference design, then scaling the input parameters appropriately and repeating the calculations.

If we assume that the geometric decorrelation is small, as it must be for our geometry and a 30 m horizontal resolution, and that the signal-to-noise ratio is high (>10 dB), we conclude that the condition $\rho < 0.001$ is easily met by our system. According to the discussion above, it is advantageous to increase the bandwidth as much as the data rate will allow. To meet our data-rate requirements, we select a bandwidth of 15 MHz, which results in an instantaneous data rate of 109 Mbit/s, and an average data rate of 44 Mbit/s. (This data rate can be

† DIXON, T. Private communication.

decreased by a factor of two if onboard range compression is used in the spacecraft.) We could obtain better performance if the bandwidth were increased, but since the data rate is proportional to Δf and it is already at the B and in the expression for the height error as a function of phase error (eqn. 31). Scaling these parameters appropriately allows calculation of the height error as a function of baseline, shown in Fig. 7*c*. The height error

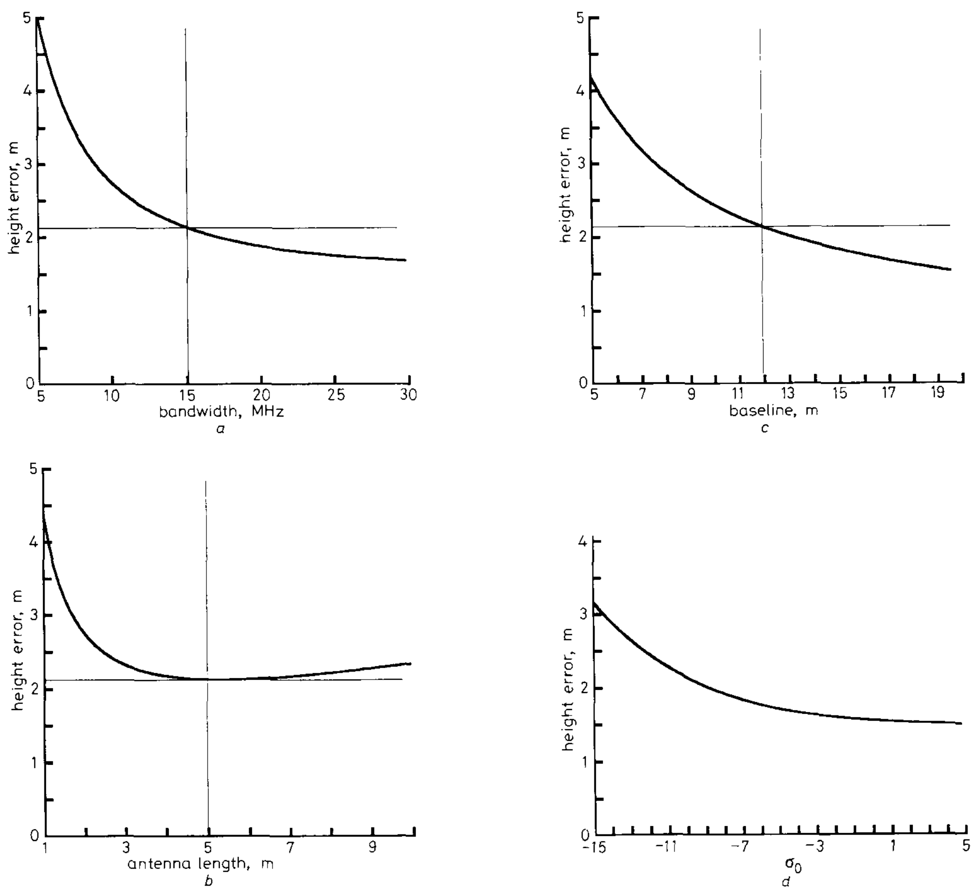

Fig. 7 *Design curves showing dependence of height error on various parameters*
For each plot, all other design parameters were held constant
a bandwidth
b antenna length
c baseline
d σ_0

maximum allowable value, we are data-rate limited in the reference system.

An examination of the previous system parameters shows that $\chi = 51.8$. According to eqn. 42 this corresponds to an optimum number of azimuth samples of 11.2 and an optimum antenna length of 5.6 m. In order to have an integer number of samples in our resolution cell, and to minimise antenna storage and deployment problems, we select a 5 m antenna. As can be seen from Fig. 7*b*, this entails only a small degradation of the height error. A longer antenna would increase R_{SN}, but the decrease in N_L would compensate, so there would not be much gain in performance. A shorter antenna, however, would give up too much in R_{SN} to make up in looks, and the performance would degrade significantly.

The baseline enters the height-error calculation through the geometric decorrelation (eqn. 14) where $a_r \propto$ decreases as baseline increases, which is not surprising as the optimum baseline from eqn. 44 is

$$B_{opt} = \{1 - \gamma_{opt}(1 + R_{SN}^{-1})\} \frac{\lambda r_0 \tan \theta_0}{R} \tag{45}$$

which is 103.2 m for the reference system. Although deployable-structure-size constraints limit the baseline to < 15 m, it is important for the spacecraft designer to know that the largest possible baseline available is the most desirable. We summarise our system parameters in Table 1.

It is interesting to consider the implications of the sensitivity equations on the knowledge requirements for the baseline attitude and the baseline length. If we allow the attitude-height error to be or the order of 1 m, we obtain the following requirement on the attitude know-

Table 1: System parameters

Orbit height	400 km
Look angle	30°
Baseline tilt	30°
Baseline length	12 m
Frequency	35 GHz
Polarisation	VV
Transmit power	250 W
Pulse length	80 μs
Bandwidth	15 MHz
PRF	4kHz
Pulse timing	interleave mode
Antenna size	0.45 m × 5 m
Antenna beamwidths	$9.9° \times 10^{-2} \times 1.1°$
Antenna peak gain	52.8 dB
σ_0	−10 dB
Transmit loss	2.5 dB
Receive loss	1.0 dB
Atmospheric loss (2 way)	2.0 dB
Receiver noise figure	4 dB
Noise temperature	917 K
Signal-to-noise ratio (with quantisation)	11.9 dB
Data rate (raw/average)	109 Mbit/s/43.5 Mbit/s
Data rate with onboard compression	54.5 Mbit/s/21.8 Mbit/s

Table 2: Random height error for sample InSAR system, and 30 m × 30 m resolution element. Note that error would drop by a factor of 3.3 if resolution element were 100 m × 100 m, and by a factor of 16.7 if resolution element were 500 m × 500 m

Surface type	Random height error (m)		
	5% occurrence level	median value	95% occurence level
Dry snow	1.5	1.5	2.2
Wet snow	1.5	1.7	3.2
Soil and rock surfaces	1.8	1.9	5.6
Grasses	1.7	1.9	2.4
Shrubs	1.7	1.8	2.2
Short vegetation	1.6	1.8	2.4
Trees	(unknown)	2.4	(unknown)

Table 3: Systematic (or long-wavelength) height errors for various mean surface slopes. Slope direction is chosen to maximise height error in each case.

Error source	Systematic height error (m)		
	0° slope	10° slope	20° slope
Baseline knowledge	0.2	0.3	0.3
Attitude knowledge	1.1	1.4	1.7
Clock timing	0.1	0.1	0.1
Ephemeris horizontal	0	0.2	0.4
Ephemeris vertical	0.1	0.1	0.1
Atmospheric/ ionospheric errors	0.2	0.2	0.2

ledge from eqn. 30 (assuming zero surface slope)

$$\delta\xi \leq \frac{\delta z}{r} \simeq 1 \text{ arcsec} \tag{46}$$

This is a very stringent requirement, but not beyond the capabilities of current star trackers, such as the Astros-1. On the other hand, the differential error across the swath is less than 10 cm, so that the attitude height error can be considered as a mere vertical shift in the topography, and can easily be corrected with the presence of only one tie point. The precision of the height measurement is not affected by this error, only its accuracy, so that local topography, needed for hydrologic studies, for instance, will not be affected.

We derive the requirement for baseline-length determination by bounding the height error at the edge of the swath (recall that, at the centre of the swath, the baseline height error vanishes to first order for a tilted baseline). The requirement is then given by

$$\delta B \leq \frac{B\delta z}{r \tan(\theta_{bw}/2) \sin\theta} \tag{47}$$

where θ_{bw} is half the 3 dB beamwidth, which in our case is given by $\theta_{bw} = 0.55°$. This results in a requirement on the baseline error to be less than 5 mm, for 1 m height error, or 1 mm for a 20 cm height error. These requirements for control and stability of the baseline are easy to satisfy with present technology.

The height error as a function of backscatter cross-section is shown in Fig. 7*d*, and is easily calculable, since σ_0 only impacts the signal-to-noise ratio, which in turn affects the height error through γ. In our nominal design, we have assumed a σ_0 of −10 dB. As expected, height error is a monotonically decreasing function of σ_0, but only relatively small gains in performance are obtained if σ_0 increases by more than 3 dB from the reference system, while decreases in σ_0 produce more significant error increases. In Tables 2 and 3, we present the expected system performance as a function of measured values of σ_0 for various terrain types at 35 GHz. The data used were obtained from the reference volume by Ulaby and Dobson [12].

7 Simulation results

The theoretical results previously presented apply to surfaces which can be locally modelled as tilted planes in the neighbourhood of the resolution cell. A major unknown in the performance is, then, the presence of nonlinear topographic features. Of course, the ultimate test of any theory is experiment, but it is extremely difficult to find well characterised surfaces and well calibrated radar systems to carry out such a verification. On the other hand, simulation of the scattering and analysis process provides a high degree of control over surface and system parameters, as well as performance estimates for different topographies. The reasons for simulation are thus twofold: first, to verify theoretical predictions of height error as functions of radar and surface parameters; and secondly, to determine the performance of the system under more realistic, dynamic conditions of changing terrain.

The simulation proceeds in two major steps: generation of the complex images received by each antenna; and processing those images to produce a height map. The generation of the images begins with a digital elevation map (DEM) consisting of heights on a 30 × 30 m grid. To simulate distributed natural targets, we assume that the SAR return can be modelled as the coherent addition of many scatterers which are small compared with the resolution cell size, but large compared with the wavelength, so that the return from each individual scattering centre has circular Gaussian statistics. This last assumption is not necessary, and we have found that the results do not change if the scattering centres are modelled as deterministic reflectors, and the number of reflectors per resolution cell exceeds about ten. However, by starting with Gaussian statistics, we ensure that the statistics of the return signal are Gaussian.

Because the scattering centres are assumed to be much smaller than the SAR-resolution cell size, we can model the return from each individual scattering centre as a point-target response. For this work we assume that the point-target response is given by eqn. 12. However, the simulation has the capability of incorporating nonideal point-target responses, thus allowing the study of nonideal-InSAR-system errors, such as receiver imbalance and yaw errors. We intend to report on these results in the future. In addition, the simulation incorporates shadowing, thermal noise and possible variations of σ_0 with incidence angle and terrain. Since the SAR system is linear, the return from many point targets can be obtained by coherently summing the return from all the individual point targets. To simulate a homogeneous point target, we sprinkle scattering centres uniformly between the points of the DEM. Initially, the scatterer heights are obtained by linear interpolation between DEM points. An additional random-height component, to simulate surface roughness smaller than the DEM resolution, may be generated if desired. For the examples presented here, we chose a density of 1/3 points per square metre, or, equivalently, 16.7 points per one-look-SAR resolution cell. The ideal point-target return has infinite extent, but decays quickly. In the results presented below, we have chosen to truncate the point-target response after the seventh lobe, in both azimuth and range, to minimise computation time. In addition, since the effect of thermal noise is well understood, we have looked at the infinite R_{SN} case, where the signal decorrelation is completely determined by the geometric-decorrelation factor, which is the true limitation of InSAR systems.

The processing step begins after the generation of the two simulated-SAR complex images. First the two images are coregistered, and the product of the complex images over the number of azimuth looks is averaged as in eqn. 24. This provides phase-difference estimates on $[0,2\pi]$ over the image. This wrapped phase is then unwrapped starting at the centre (for which $\hat{\Phi} \simeq 0$ and $z = 0$ by construction) using the algorithm of Goldstein *et al.* [11]. We note here that other algorithms which take account of the amplitude as well as the phase of the complex image product [13] may also be used at this step, but since no rigorous error analysis has been presented for any of the proposed algorithms we have selected the simplest one. Research is continuing in this area. After unwrapping, the heights are estimated at each point using the known geometry and eqns. 26 and 27. Finally the resulting height map is rectified, interpolated to a 15 m grid, and averaged to yield height estimates on the same 30 × 30 m grid as the source DEM.

The significant difference between distributed targets and point targets is that distributed targets decorrelate as the baseline is increased, while point targets remain correlated. As a test of our distributed target simulation, we simulated a distributed flat plane and measured the correlation between the two simulated images as the interferometer baseline was increased. The results are compared with the theoretical predictions in Fig. 8. Although the trends in this graph are nearly identical, the simulated data are always more correlated than the theory predicts and, by eqn. 31, the more correlated the phases, the lower the height error for a given baseline and geometry. It is likely that the source of this error lies either in the limited number of points per resolution element or the limited number of sidelobes of the point-target response included in the simulation. Either would produce higher correlation than would actually be observed in nature, since the sidelobes of points removed from a given range and azimuth bin tend to add-in as noise. We note, however, that the difference in height errors produced by this idealisation is only ~15 cm, and is swamped by terrain-induced errors when the RMS height is sufficiently large. In these and all the following simulations, the radar parameters are those in Table 1, with the exception of signal-to-noise ratio.

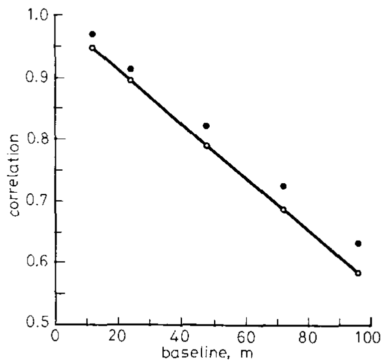

Fig. 8 *Comparison of correlation coefficients measured from simulation and estimated from eqn. 25 for baselines varying from 12 m to 96 m*
Simulation results are consistently slightly more correlated than expected from theory, for reasons discussed in the text
● simulation correlation
--○-- theoretical correlation

An interesting practical question in determining InSAR performance is the presence of surface roughness within the resolution cell. To assess the accuracy of the theoretical expressions for height error as a function of internal roughness, we compare the predictions of eqns. 2, 21, 28 and 31 with the results of simulation experiments. The heights of the scattering points were independently drawn from Gaussian distributions with varying RMS height (σ_h). The resulting height was found to be unbiased, and the error standard deviations σ_z are plotted in Fig. 9 along with the theoretical prediction.

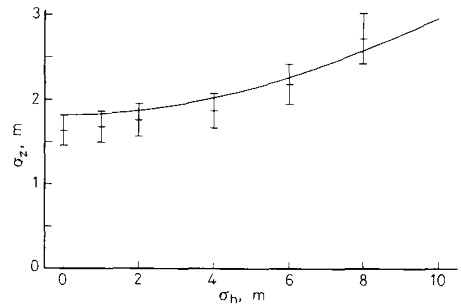

Fig. 9 *Comparison of height standard deviation measured from simulation with theoretical estimate from eqn. 31 for varying roughness at subresolution element scales*
Simulation results show lower height variance for small σ_h most likely a result of the same defects which produced the excess correlation in Fig. 8

The trend in the data is generally correct and is in agreement with the theory for large σ_h, but for small σ_h the simulations show significantly lower σ_z than the theoretical prediction. The source of this disagreement is due to the greater correlation of the simulated data, as discussed above. Notice that, even for very large internal roughness, the height performance degrades gracefully. This implies that, in contrast to radar and laser altimeters, internal roughness is not a major determinant of the InSAR height accuracy.

The behaviour of the interferometer over varying topography is very difficult to treat analytically due to the nonlinear nature of the unwrapping process and the difficulty in characterising topographic change, so here simulations play a vital role in the analysis. An important characteristic of any height-estimation system is its response to a crosstrack step in the terrain, and we have shown the results of a simulation of 5, 15 and 40 m steps in Fig. 10, where each plot shows a crosstrack cut (a

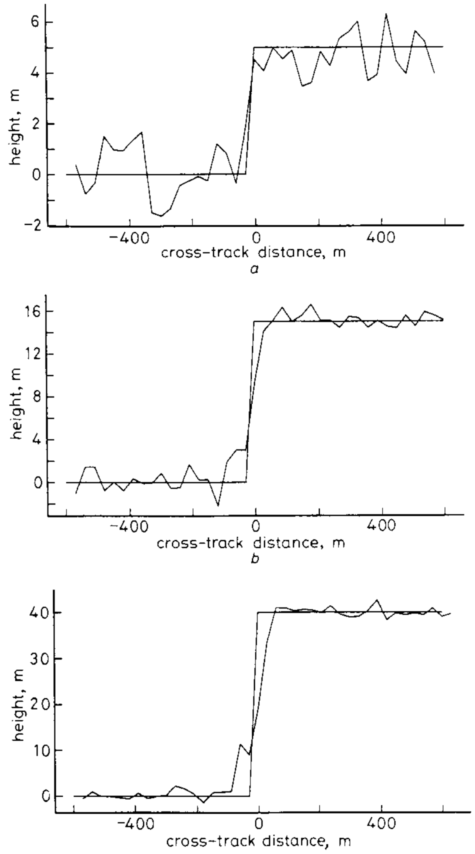

Fig. 10 *Comparison of step response of interferometer to input DEM data for various step heights*

Flat areas show error less than 2 m, but high-slope region shows errors due to interferometer response and layover (40 m step)
a 5 m step, $\langle\Delta\rangle = 0.07$ m, $\sigma_\Delta = 1.02$ m
b 15 m step, $\langle\Delta\rangle = 0.06$ m, $\sigma_\Delta = 1.48$ m
c 40 m step, $\langle\Delta\rangle = 0.002$ m, $\sigma_\Delta = 4.66$ m

single range line) in the middle of the image; the jagged curve is the simulation data and the smooth curve the DEM. The RMS height error for the 1 km surrounding the steps is 1.02 m, 1.48 m, and 4.66 m, respectively, reflecting an increasing error magnitude with increasing slope produced by the lowpass-filtering effect expecially evident in the 40 m step. The large errors for this step are produced by the complete layover of the step; the unwrapping algorithm did not fail in this case because the overall height of the step was less than Δz_{max}, the height increment which produces a phase shift of π (for the reference system, $\Delta z_{max} = 82.8$ m). Thus, we see that InSAR systems have the potential of detecting very sudden changes in elevation, consistent with their nominal horizontal resolution.

In Fig. 11 we show similar results for various 120 m long ramps of 10, 50 and 70 m heights. The RMS height errors for these simulations are 1.09 m, 1.96 m and 1.71 m, respectively. As might be intuitively expected, these errors are somewhat smaller than for the step, reflecting the smaller rate of change of slope of the ramps.

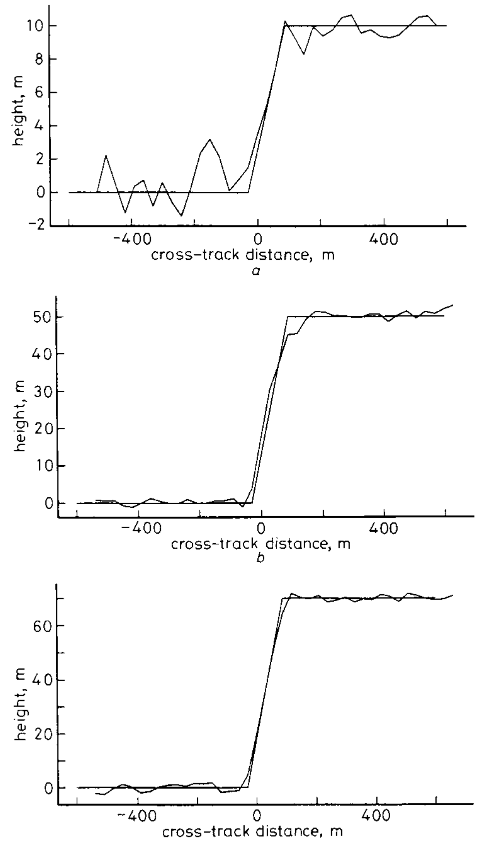

Fig. 11 *Comparison of interferometer response to a ramp with the DEM input data for various ramp lengths*

Errors are smaller than for similar height steps in Fig. 10, due to increase in slope rate of change for ramps
a 10 m ramp, $\langle\Delta\rangle = 0.22$ m, $\sigma_\Delta = 1.09$ m
b 50 m ramp, $\langle\Delta\rangle = 0.36$ m, $\sigma_\Delta = 1.96$ m
c 70 m ramp, $\langle\Delta\rangle = 0.06$ m, $\sigma_\Delta = 1.71$ m

Note that the 70 m ramp is completely laid over, so there really is no height information over most of that ramp; small variations in height within that ramp would be invisible. A 90 m ramp was not only laid over, but also caused the unwrapping algorithm to fail, as expected since this increment is greater than Δz_{max}. Overall, therefore our experience with these idealised steps and ramps, for which the average error is generally less than 2 m, suggests that the interferometer might follow real terrain quite accurately.

To determine the interferometer performance on real terrain, we selected as input DEMs two sections of a USGS 7 1/2 minute DEM for Kilauea volcano on Hawaii, with nominal 30 m horizontal resolution and 7 m vertical accuracy. The sections were 2.4 km in azimuth and 10 km in range (a full swath), and were chosen to reflect two kinds of topographic change.

Region A, which represents the transition of the Kau desert onto the Keamoku lava flow, is characteristic of long-wavelength topographic changes with small surface slope. Region B, which consists of the transition between the Kau desert and Kilauea crater, and includes the very steep Keanakakoi and Halemaumau craters, is characteristic of regions with very sudden changes in surface height and slope. Fig. 12 shows the results from A and

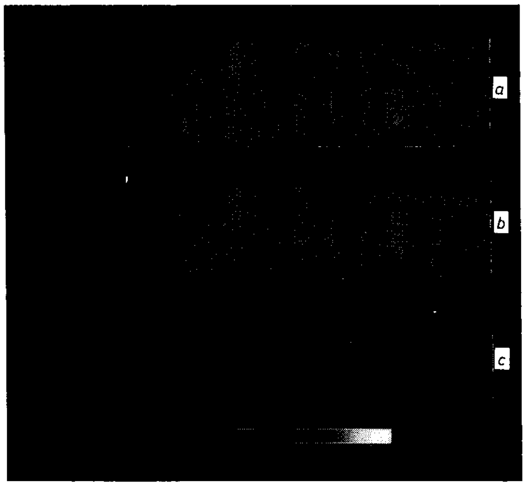

Fig. 12 *Results from region A*
a left-hand numerical derivative of the input DEM (to simulate side lighting)
b simulation height map similarly presented
c height difference, grey scale runs from −25 m to +25 m

Fig. 13 those from B. In each Figure, the upper image is the left-hand numerical derivative of the input DEM (to simulate side lighting), the middle image is the simulation

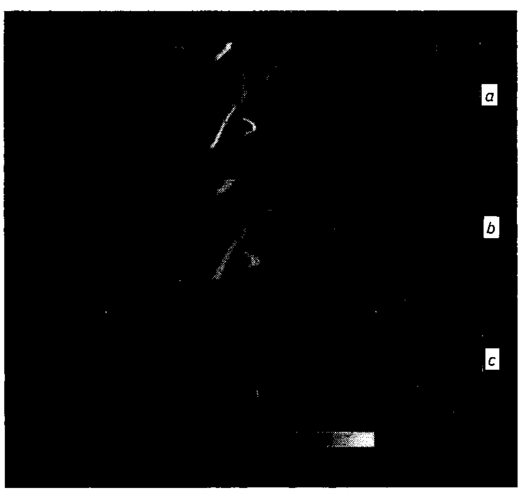

Fig. 13 *Results from region B*
Presentation similar to that in Fig. 12

height map similarly presented, and the bottom image is the height difference where the grey scale runs from −25 m to +25 m. For region A, the height noise is visible in the simulation image when compared in the smoothest sections to the DEM, but the error image shows little structure. A cut through the DEM and the simulation height results and their difference for A are plotted in Fig. 14*a*, which clearly indicates that the height

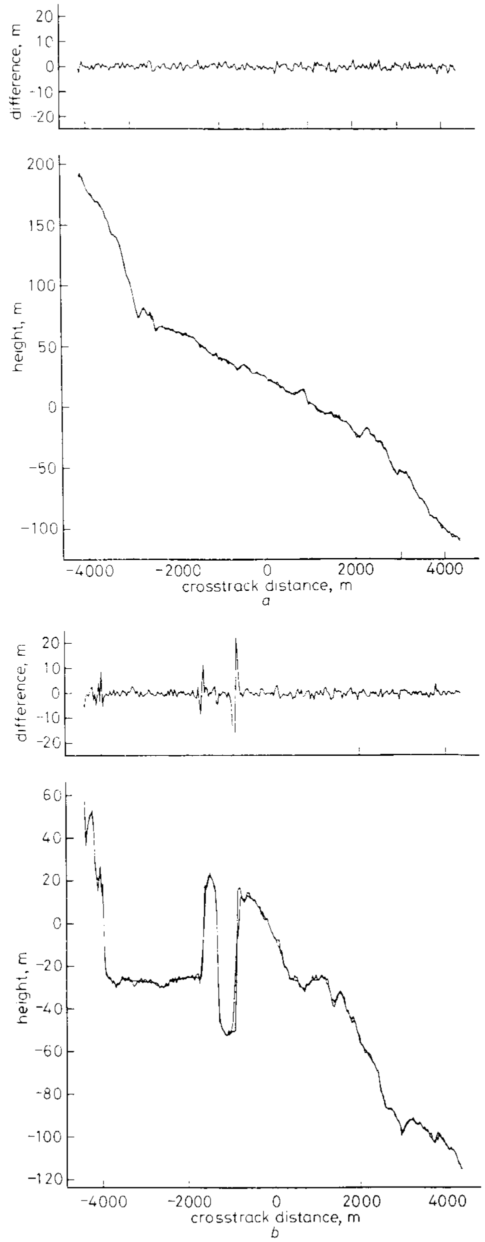

Fig. 14 *Comparison of interferometer height estimates with DEM input data for two areas on Kilauea, Hawaii*
In each case a single range line is shown, as well as the difference between the input and interferometer estimates shown above it. Data are extracted from the images in Figs. 12 and 13
a region A, smooth terrain on a lava flow
b region B, rough terrain with Kilauea Crater and other craters

estimates track the DEM very well and the magnitude of the error is generally less than 2 m and often much smaller, consistent with an overall $\sigma_z = 1.11$ m.

The more extreme terrain of B, which included some rather steep crater walls (up to 52° and 65 m high) produced much greater errors in those regions of high slope, as shown by the very dark and light areas of the difference image in Fig. 13, which correspond to the high-slope features in the DEM and simulation height images above it. The lowpass nature of the simulation results is clearly evident on the crater walls, similar to the step and ramp responses measured previously, and in Fig. 14B, which shows the range line in region B running through the Kilauea and Keanakakoi craters in the lower middle of the image. This figure shows that the errors, which at peak may be greater than 25 m in magnitude, still are localised to the steeply sloping regions, and away from those areas the RMS error is similar to that in A. The overall average RMS height difference, even for the extreme topography of region B, is still only 1.8 m.

The concentration of error in the regions of large slope may be verified by binning the height error against local slope for each region. The results are plotted in Fig. 15;

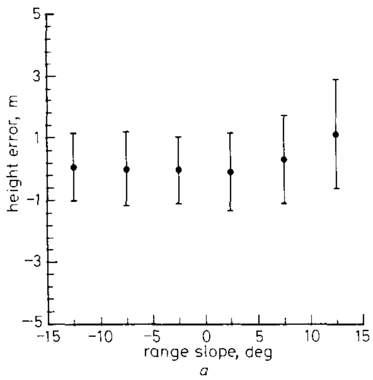

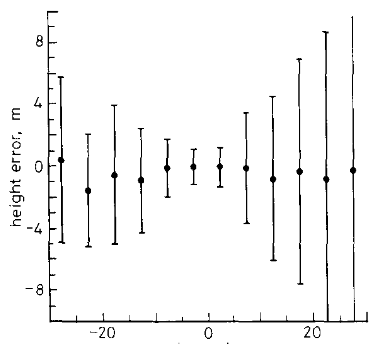

Fig. 15 *Mean and standard deviation of height error as a function of local slope*

Estimates are unbiased and standard deviations show little dependence on slope for smooth topography, but much greater dependence for more extreme topography of region B
a region A
b region B

the mean error is plotted and the RMS height variation is indicated by the error bars. For region A, $\sigma_z \simeq 1$ m with very little dependence on local slope, but a much greater dependence of the error on local slope is evident in region B. In both cases the mean height appears to be unbiased. These results suggest that, in the rougher terrain, the local slope is correlated with the large-scale surface curvature, which is itself directly related to the height error, while in the smoother terrain local slope is dominated by local fluctuations which swamp the rather small large-scale surface curvature. The error for positive slopes is also expected to be greater than for negative slopes, because only positive slopes may produce layover, which yields increased height error as shown previously by the 40 m step response.

8 Conclusions

We have presented a derivation of the statistical characteristics of InSAR returns which include the new effects of surface slope and roughness, vegetation and baseline tilt. Next, we presented the maximum likelihood estimator for phase noise and derived an expression for the estimation error. Using these results, we derived the InSAR-error budget and obtained a set of design criteria for optimising InSAR performance. As an illustrative example, we applied these results to design a 35 GHz InSAR system capable of providing global mapping in less than one year with horizontal resolution and height accuracy and precision which meet most of the stringent scientific requirements. Finally, we verified our theoretical predictions by simulation and examined the effect of sudden changes in the topography on the interferometer height error. We conclude that interferometric mapping provides an accurate high-resolution topographic system which is capable of operating even over severe topography.

9 Acknowledgment

The authors thank Soren Madsen for carefully reviewing the manuscript, and our Italian colleagues Sergio Vetrella, Antonio Moccia, and Roberta Bertoni for fruitful discussions. The research described was carried out under contract with the National Aeronautics and Space Administration.

10 References

1 Topographic Science Working Group report to the Land Processes Branch, Earth Science and Applications Division, NASA Headquarters'. Lunar and Planetary Institute, Houston, 1988
2 GRAHAM, L.C.: 'Synthetic interferometer radar for topographic mapping', *Proc. IEEE*, 1974, **62**, (6), pp. 763-768
3 ZEBKER, H.A., and GOLDSTEIN, R.M.: 'Topographic mapping from interferometric synthetic aperture radar observations', *J. Geophys. Res.*, 1986, **91**, pp. 4993–4999
4 LI, F.K., and GOLDSTEIN, R., 'Studies of multibaseline spaceborne interferometric synthetic aperture radars', *IEEE Trans.* 1990, **GE-28,** (1), pp. 88–98
5 ELACHI, C.: 'Spaceborne radar remote sensing: applications and techniques' (IEEE Press, 1988)
6 MOCCIA, A., and VETRELLA, S.: 'A tethered interferometric SAR for a topographic mission', submitted to *IEEE Trans. Geoscience and Remote Sensing*, 1990
7 TSANG, L., KONG, J.A., and SHIN, R.T.: 'Theory of microwave remote sensing' (Wiley-Interscience, New York, 1985)
8 GOODMAN, J.W.: 'Statistical optics' (Wiley-Interscience, New York, 1985)
9 RODRIGUEZ, E.: 'Altimetry for non-Gaussian oceans: height biases and estimation of parameters', *J. Geophys. Res.*, 1988, **93,** C11, 14,107–14,120
10 RODRIGUEZ, E.: 'Maximum likelihood estimation of the interferometric phase from distributed targets', *IEEE Trans.*, **GE** (to be published)
11 GOLDSTEIN, R.M., ZEBKER, H.A., and WERNER, C.L.: 'Satellite radar interferometry: two-dimensional phase unwrapping', *Radio Science*, 1988, **23**, (4), pp. 713-720
12 ULABY, F.T., and DOBSON, M.C.: 'Handbook of radar scattering statistics for terrain' (Artech House, Boston, 1989)
13 PRATI, C., ROCCA, F., MONTI GUARNIERI, A., and DAMONTI, E.: 'Seismic migration for SAR focusing: interferometric applications', *IEEE Trans.*, 1990, **GE-28,** pp. 627–639